NSTX-U THEORY, MODELING AND ANALYSIS RESULTS

S.M. KAYE[1], D.J. BATTAGLIA[1], D. BAVER[2], E. BELOVA[1], J.W. BERKERY[3], C.S. CHANG[1], A. DIALLO[1], V. DUARTE[1], N. FERRARO[1], E. FREDRICKSON[1], N. GORELENKOV[1], W. GUTTENFELDER[1], W. HEIDBRINK[4], D. KIM[1], I. KREBS[1], S.-H KU[1], J. LESTZ[1], R. LAHAYE[5], D. LIU[4], L. MORTON[5], J. MYRA[2], D. PFEFFERLE[1], M. PODESTÀ[1], Y. REN[1], J. RIQUEZES[3], S.A. SABBAGH[3], F. SCOTTI[6], V. SOUKHANOVSKII[6], T. STOLTZFUS-DUECK[1], , J.-W. AHN[7], J.P. ALLAIN[8], R. BARCHFELD[9], A. BHATTACHARJEE[1], F. BEDOYA[8], R.E. BELL[1], N. BERTELLI[1], M.D. BOYER[1], D. BRENNAN[10], G. CANAL[5], J. CANIK[7], N. CROCKER[11], D. DARROW[1], L. DELGADO-APARICIO[1], C. DOMIER[9], F. EBRAHIMI[1], T. EVANS[5], R. FONCK[12], H. FRERICHS[12], K. GAN[13], S. GERHARDT[1], T. GRAY[7], T. JARBOE[14], S. JARDIN[1], M.A. JAWORSKI[1], R. KAITA[1], D.M. B. KOEL[10], E. KOLEMEN[10], KRIETE[12], S. KUBOTA[11], B.P. LEBLANC[1], F. LEVINTON[15], N. LUHMANN[9], R. LUNSFORD[1], R. MAINGI[1], R. MAQUEDA[16], J.E. MENARD[1], D. MUELLER[1], C.E. MYERS[1], M. ONO[1], J.-K. PARK[1], R. PERKINS[1], F. POLI[1], R. RAMAN[14], M. REINKE[7], T. RHODES[11], C. ROWLEY[10], D. RUSSELL[2], E. SCHUSTER[18], O. SCHMITZ[12], Y. SECHREST[15], C.H. SKINNER[1], D.R. SMITH[12], B. STRATTON[1], G. TAYLOR[1], K. TRITZ[19], W. WANG[1], Z. WANG[1], I. WATERS[12], B. WIRTH[13] AND S.J. ZWEBEN[1]

1 Princeton Plasma Physics Laboratory, Princeton University, Princeton, NJ 08543, United States of America
2 Lodestar Research Corporation, Boulder, CO, United States of America
3 Columbia University, New York, NY, United States of America
4 University of California at Irvine, Irvine, CA, United States of America
5 General Atomics, San Diego, CA, United States of America
6 Lawrence Livermore National Laboratory, Livermore, CA, United States of America
7 Oak Ridge National Laboratory, Oak Ridge, TN, United States of America
8 University of Illinois at Urbana-Champaign, Urbana, IL, United States of America
9 University of California at Davis, Davis, CA, United States of America
10 Princeton University, Princeton, NJ, United States of America
11 University of California at Los Angeles, Los Angeles, CA, United States of America
12 University of Wisconsin, Madison, WI, United States of America
13 University of Tennessee, Knoxville, TN, United States of America
14 University of Washington, Seattle, WA, United States of America
15 Nova Photonics, Princeton, NJ, United States of America
16 X Science LLC, Plainsboro, NJ, United States of America
17 University of Michigan, Ann Arbor, MI, United States of America
18 Lehigh University, Bethlehem, PA, United States of America
19 Johns Hopkins University, Baltimore, MD, United States of America

e-mail contact of main author: kaye@pppl.gov

Abstract

The mission of the spherical tokamak NSTX-U is to explore the physics that drives core and pedestal transport and stability at high-β and low collisionality, as part of the development of the ST concept towards a compact, low-cost ST-based Pilot Plant. NSTX-U will ultimately operate at up to 2 MA and 1 T with up to 10 MW of Neutral Beam Injection (NBI) power for 5 seconds. NSTX-U will operate in a regime where electromagnetic instabilities are expected to dominate transport, and beam-heated NSTX-U plasmas will explore energetic particle (EP) parameter space that is relevant for both α-heated conventional and low aspect ratio burning plasmas. NSTX-U will also develop the physics understanding and control tools to ramp-up and sustain high performance plasmas in a fully-noninductive fashion. NSTX-U began research operations in 2016, but a failure of a divertor magnetic field coil resulted in the suspension of operations and initiation of Recovery activities. During this period, there has been considerable work in the area of analysis, theory and modeling with a goal of understanding the underlying physics to develop predictive models that can be used for high-confidence projections for both ST and higher aspect ratio regimes. The studies have addressed issues in thermal plasma transport, EP-driven instabilities at ion-cyclotron frequencies and below, macrostability, and edge and divertor physics.

1. INTRODUCTION

The mission of the spherical tokamak NSTX-U [1] is to explore the physics that drives core and pedestal transport and stability at high-β and low collisionality, as part of the development of the ST concept towards a compact, low-cost ST-based Pilot Plant [2]. NSTX-U will operate at up to 2 MA and 1 T with up to 10 MW of Neutral Beam Injection (NBI) power for 5 seconds. NSTX-U will study electromagnetic instabilities, which are expected to dominate transport in the core and neutral beam-energetic particle (EP) phase space that is relevant for both α-heated conventional and low aspect ratio burning plasmas. At high-β, virulent non-linear EP-driven instabilities are expected to occur, and NSTX-U will be developing means to suppress or mitigate the modes through tailored NB injection and to develop models to predict the enhanced EP transport caused by these modes. NSTX-U will also develop the physics understanding and control tools to ramp-up and sustain high performance plasmas in a fully-non-inductive regime, aided by the flexible aiming of the NBI-system for current and rotation control.

NSTX-U began research operations in 2016, producing 10 weeks of commissioning and scientific results [3, 4]. However, a number of technical issues, including the failure of a key divertor magnetic field coil, resulted in the suspension of operations and initiation of Recovery activities. During this period, there has been considerable work in the area of analysis, theory and modeling with a goal of understanding the underlying physics to develop predictive models that can be used for projections for both ST and higher aspect ratio regimes. This paper will discuss results of these studies in the areas of confinement and transport, energetic particle physics, macrostability, and edge and divertor physics.

1. CORE PHYSICS: TRANSPORT AND CONFINEMENT

1.1. Gyrokinetic analysis of L-Mode plasmas

Local nonlinear gyrokinetic simulations run for an NSTX L-mode [5] predicted ion-scale transport that peaked at very large values around ρ=0.6 (Fig. 1a-b). However, there is a rapid reduction in transport on either side of this peak due to (i) E×B shearing rates becoming larger than linear growth rates towards the core, and (ii) a reduction in the gyroBohm coefficient Q_{GB}~$T^{5/2}$ towards the edge. Global nonlinear ion scale simulations using GTS [6] predict a much smoother variation of transport as a consequence of profile shearing effects. With neoclassical transport added, the global simulations reproduce ion thermal transport comparable to experiment when neoclassical transport is added to the calculated turbulent transport. However, predicted electron heat flux in the global simulations is negligible indicating that some physics is still missing.

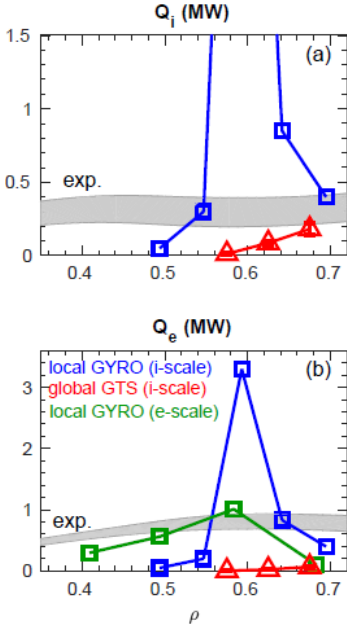

Fig. 1 Comparison of simulated and experimentally inferred (a) ion and (b) electron thermal heat fluxes.

Linear analysis predicts ETG modes to also be unstable, and local, nonlinear ETG simulations that resolve only electron-scale turbulence have been run. As seen in Fig. 1b, the ETG simulations predict significant transport around the mid-radius, approaching experimental levels. Given the similarity in electron heat flux at electron scales and ion heat flux at ion scales from global simulations ($Q_{e,\ high\text{-}k}$~$Q_{i,\ low\text{-}k}$), cross-scale coupling effects cannot be ruled out. The potential importance of multiscale effects is further supported by noting that the ratio of the maximum γ/k_y predicted from the electron-scale instability is comparable to or exceeds that predicted for the ion-scale instability. This metric has been proposed as a criterion for indicating the potential importance of multi-scale effects.

1.2. L-H snd H-mode physics

A database of diverted discharges from the 2016 operation of NSTX-U was used to identify the target conditions for reliable H-mode access during ramp-up when using 3 to 5 MW of NBI heating. The set of criteria that were identified included: line-averaged density exceeding 1.25×10^{19} m^{-3}, surface voltage of the plasma < 1.15 V, shape close to double null, and oxygen content of the below a critical threshold. The results suggest it is unlikely to trigger an L-H transition with only two criteria met but very likely when satisfying all four. These results can influence the development of the target boundary shape, neutral fueling and loop voltage evolution during operations, and can lead to reliable triggering of the L-H transition early in the I_p ramp.

The dynamics across the L-H transition in NSTX discharges was studied using computed velocity fields of turbulence measured by the gas-puff imaging (GPI) diagnostic [7]. While the relative GPI turbulence amplitude decreased across the L-H transition, no consistent changes preceding the transition in relative fluctuation level, average poloidal and radial correlation lengths and velocities, or average poloidal flow shear were observed. While these turbulence quantities are different from before to after the transition, there is no "trigger" that would help identify the L-H transition mechanism.

The energy exchange between turbulence and mean flows was computed from the time varying 2D velocity fields of the GPI-measured turbulence. It was found that, consistently, the energy transfer 1 cm inside the separatrix went from the mean flow to the turbulence just before the L-H transition. This is seen in Fig. 2, where the production term, related to the Reynolds work and the transport of energy to/from non-zonal turbulent flows, is negative, indicating an energy flow from mean flows to turbulence, inconsistent with the predator-prey model [8]. Furthermore, in order for the energy transfer to mean flows to be large enough to deplete the turbulence, the ratio of kinetic energy in the mean flow to the thermal free energy in the turbulence must be near 1. This ratio, however, was found to be of order 10^{-2} in NSTX, suggesting that direct turbulence depletion by Reynold's work is not large enough to explain the L-H transition, again contrary to the standard predator-prey model. This suggests that the direct turbulence suppression by Reynolds work may not be large enough to explain the L-H transition on NSTX, to within the uncertainties in the analysis and interpretation of the 2D velocity fields [7].

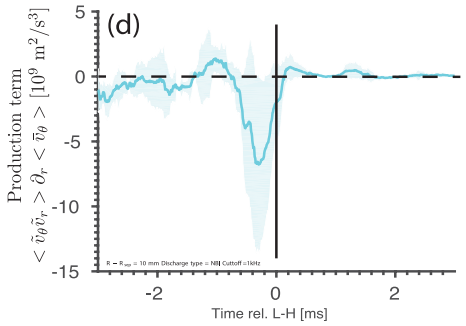

Fig. 2 Production term, measuring energy flow between mean flow and turbulence, as a function of time across the L-H transition (vertical line). A negative production term indicates energy flow from mean flow to turbulence.

The Enhanced Pedestal (EP) H-mode [9] features the development of a wider H-mode pedestal with a significant increase in the ion temperature and carbon rotation gradients in an ELM- and MHD-free period following a large ELM. These discharges achieve improved energy and momentum confinement with a beneficial decrease in the impurity accumulation relative to a standard ELM-free H-mode regime. Recent analysis of EP H-mode discharges demonstrates that the transport bifurcation is triggered by a transient period of lower collisionality during the ELM recovery where the ∇T_i increases consistent with neoclassical ion thermal transport. The transient period of larger ∇T_i reinforces the lower edge collisionality via a reduction of the neoclassical impurity pinch and movement of the region of large E_r shearing rate toward the core. These effects lead to a wider density pedestal providing access to larger pedestal pressures that are stable to peeling instabilities. The larger ∇T_i also acts to stabilize electron-scale turbulence, improving the edge electron thermal barrier.

2. ENERGETIC PARTICLE PHYSICS

2.1. Energetic particle-modified GAE modes

Spherical tokamaks like NSTX/NSTX-U routinely operate with super-Alfvénic beam ions, and the concomitant broad spectrum of fast-ion driven instabilities. Fully self-consistent hybrid MHD/particle simulations reveal strong energetic particle modifications to sub-cyclotron global Alfvén eigenmodes (GAE) in low-aspect ratio, NSTX-like conditions [10]. Linear simulations were run with HYM [11], an initial value code in full 3D toroidal geometry in which a single-fluid thermal plasma is coupled to full orbit kinetic fast ions, with self-consistent evolution of the MHD equilibrium.

In this set of simulations, key parameters defining the beam-like fast ion distribution function – the normalized injection velocity and central pitch – were varied in order to study their influence on the characteristics of the excited modes. It was found that the frequency of the most unstable mode for each toroidal harmonic changes significantly and continuously with beam parameters, depending most substantially on the injection velocity, as shown in Fig. 3. This unexpected result is present for both co- and counter-propagating GAEs, where the linear dependence and sign of the change are consistent with the Doppler-shifted cyclotron resonances, which drive the modes. There are no clear concurrent changes in mode structure that would indicate that these frequencies correspond to distinct eigenmodes. Furthermore, it was found that equilibrium changes themselves were an order of magnitude too small to account for the frequency dependence on injection velocity. Numerical evaluation reveals that the mode growth rate is maximized when the parallel resonant velocity is a fixed fraction of the injection velocity, independent of the injection velocity, which suggests a linear relationship between the injection velocity and parallel resonant velocity. This energetic-particle-modified GAE may be the first instance of an energetic particle (EP) mode driven by the cyclotron resonance and excited at an appreciable fraction of the cyclotron frequency instead of near EP orbital frequencies.

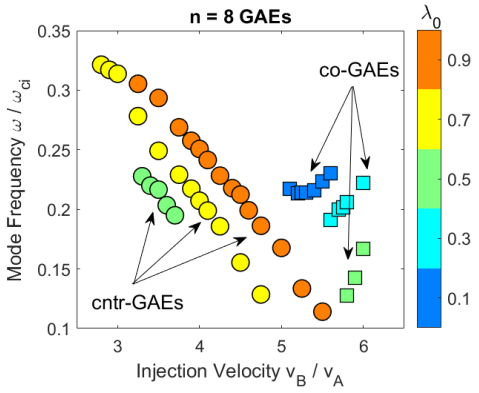

Fig. 3 Change in frequency for |n|=8 GAEs as a function of the normalized beam injection velocity. Cntr-GAEs are marked by circles, co-GAEs by squares. Color denotes the central pitch $\lambda_0 = \mu B_0/\varepsilon$ of the beam distribution in each simulation. On-axis cyclotron frequency is 2.4 MHz.

2.2. GAE suppression by off-axis neutral beam injection

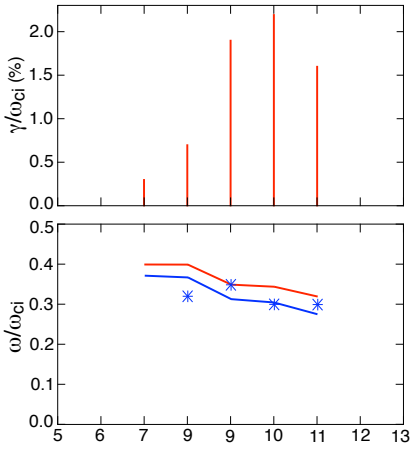

Fig. 4 Growth rates and frequencies of unstable counter-GAEs from simulations as function of toroidal mode number. Blue line is Doppler-shift corrected frequencies, points – experimental values.

Multiple GAE with a range of toroidal mode numbers and frequencies are commonly observed in beam-heated NSTX plasmas. The GAEs propagate counter to the tangentially injected beam ions and are excited through an ion cyclotron resonance with the co-moving beam ions. An analytic theory describing the Doppler-shifted ion cyclotron resonance drive for the GAE [12] predicts the scaling of the GAE frequencies and toroidal mode numbers.

This ubiquitous mode was completely suppressed with the judicious injection of a relatively small amount of fast ions injected nearly parallel to the magnetic field, *i.e.*, $V_{||}/V \approx 1$, from the new, tangential neutral beam on NSTX-U [13]. HYM simulations have been used to reproduce the experimental findings [14]; before additional beam injection the simulations show unstable counter-rotating GAEs with toroidal mode numbers n=-7 to -11, and frequencies that match the experimentally observed unstable GAEs (Fig. 4). The calculated growth rates (Fig.4 top) for the most unstable GAEs with n=-10 and -11 are about 2 to 3 times higher than that estimated from the experimental data, probably due to an underestimated damping by the bulk plasma MHD model. Nonlinear simulations show the peak saturation amplitudes of $\delta B/B_0$~1 to 5×10^{-3}, comparable to experimental estimates. HYM simulations also show that off-axis

neutral beam injection strongly suppresses all unstable GAEs even for a relatively weak added beam. Simulations found that the unstable n=-11 GAE is stabilized when fraction of the additional beam ions is larger than 7%. It is found that a complete stabilization of all unstable GAEs (n=-7 to -11) with ~25% additional tangential beam ions

2.3. Counter-propagating TAE full phase space effects

A broad NBI deposition profile is usually thought to reduce the drive for Alfvénic instabilities by reducing the radial gradient of the EP density. However, NSTX-U scenarios with off-axis NBI show evidence that broad profiles associated with tangential and off-axis neutral beam injection could lead to the *destabilization* of Alfvénic instabilities. An example is given in Fig. 5, showing the spectrum that includes both co- and counter-current propagating TAE modes. Theory predicts the destabilization of counter-TAEs for hollow EP density profiles [15]. However, for this case counter-TAEs are observed at times for which TRANSP/NUBEAM predict a peaked or flat EP density profiles. TAE stability was investigated in TRANSP through the reduced 'kick' model [16, 17]. Potentially unstable eigenmodes are first identified via the NOVA-K code. The EP response to each mode is then investigated through the orbit-following code ORBIT. The results are combined to form a 'transport probability matrix', used in the NUBEAM module of TRANSP to introduce enhanced EP transport by the instabilities and to infer mode stability [17].

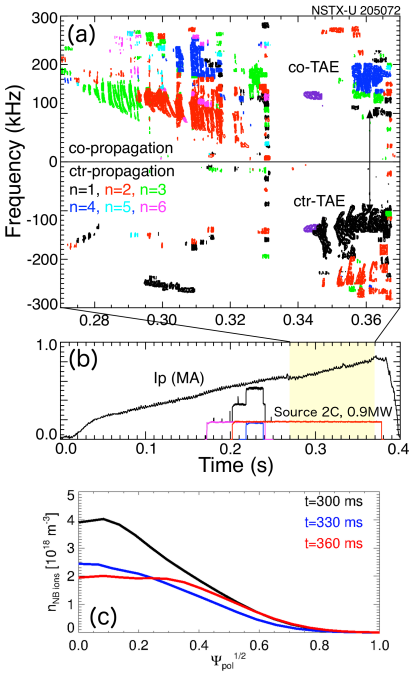

Fig. 5 (a) Toroidal mode number spectrum for co- and counter-propagating TAEs. (b) Waveforms of plasma current and NB injected power. (c) Fast ion density profile at three different times from TRANSP/NUBEAM.

Results of TAE stability analysis at two different times are shown in Fig. 6. The predicted unstable spectrum of TAEs is in reasonable agreement with the experimental observations, including a transition from co-TAEs only at earlier times to co- and counter-TAEs after t=340ms. Furthermore, the TRANSP and kick model analysis indicates that instabilities are driven by a combination of both radial *and* energy gradients in the EP distribution function [18]. The mechanisms for wave-particle interaction revealed by the energetic particle phase space resolved analysis are the starting point to identify strategies to mitigate or suppress the observed instabilities, e.g. by varying the injected NBI mix to populate EP phase space regions where wave-particle resonant interactions are reduced.

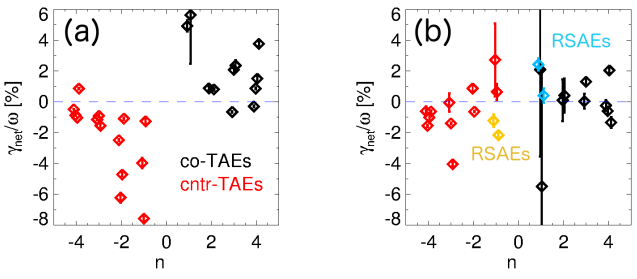

Fig. 6 Net growth rate (including damping rate from NOVA-K) for co- and counter-propagating TAEs at two different times, 340 ms (a) and 365 ms (b). The analysis recovers the transition from co-TAEs only to co- plus counter-TAEs after t=340ms, cf. Fig. 5. The predicted unstable spectrum is consistent with the experimental observations.

2.4. Role of microturbulence in TAE chirping

The spectral characteristics of Alfvén eigenmodes, such as RSAEs and TAEs, in tokamaks can vary considerably, depending on several parameters affecting their resonant interaction with fast ions [19]. When the ions can remain resonating coherently for several wave trapping (or bounce) times, the wave can evolve towards self-organizing responses; this scenario is associated with wave chirping and avalanching of several modes, leading to convective losses of fast ions. **A** criterion for the likelihood of chirping oscillations was developed based on previous analytical works on the theory of driven, kinetic instabilities near threshold with

dissipation [20-22] and evaluated for a number of NSTX, DIII-D and TFTR discharges [23-25] using the stability code NOVA-K [26]. The work predicted, and verified experimentally, that micro-turbulence can be a strong mediator between the mode transition from fixed-frequency to chirping and vice-versa. In spherical tokamaks, particles spend more time in the good curvature region and experience higher relative rotation shear. Therefore, STs naturally exhibit lower anomalous transport due to microturbulence with respect to conventional tokamaks. These distinct turbulence features have been found to explain why chirping instabilities are rare in conventional tokamaks and common in spherical tokamaks since the turbulence acts to effectively increase the scattering experienced by the resonant fast ions [27] and therefore to prevent the chirping and avalanching responses.

In order to improve the evaluation of the criterion for chirping onset, NSTX discharges that show toroidicity-induced Alfvén waves transitioning from constant frequency to chirping have been analyzed with the gyrokinetic code GTS. The δf particle-in-cell nonlinear electrostatic ion temperature gradient and trapped electron mode simulations included fully kinetic electrons and plasma profiles which were input from TRANSP [28]. The global simulations covered a range in the normalized square root of the toroidal flux from 0.2 to 0.8. The simulation results, shown in Fig. 7 support the theoretical prediction that a marked decrease in turbulence-driven EP transport causes the onset of chirping.

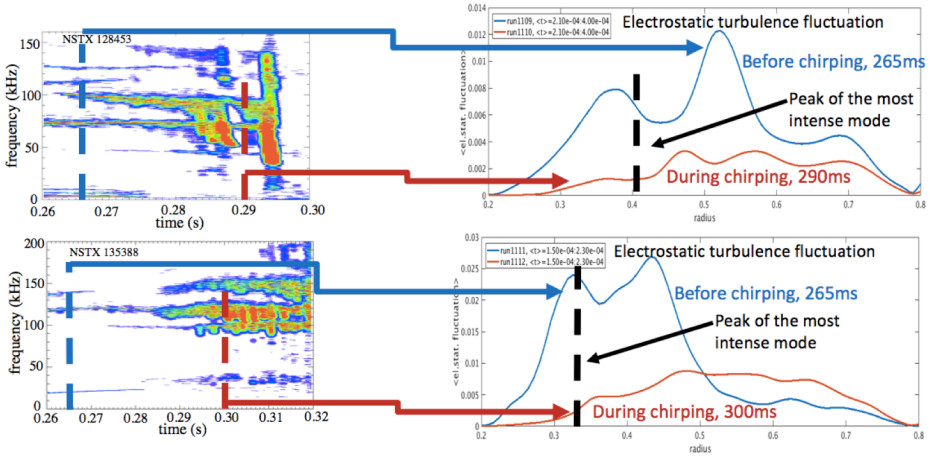

Fig. 7 Correlation between mode transition from fixed-frequency to chirping spectral response (left plots) and a marked drop of the electrostatic turbulent potential calculated by GTS (right), for NSTX shots 128453 and 135388. Reproduced from [29].

2.5. **Fast ion distribution by sawteeth on NSTX-U**

In the NSTX-U's 2016 campaign, 2-second long L-mode sawtoothing discharges were routinely achieved. Repetitive drops in neutron rate accompanied by increases of edge D_α emission were observed at each sawtooth event (Fig. 8b), suggesting that fast ions were lost or redistributed, in addition to the redistribution of thermal plasma as a result of the flux reconnection. It was observed on both the solid-state neutral particle analyzer (SSNPA) and fast ion D_α (FIDA) diagnostics that passing particles were strongly expelled from the plasma core to the edge during sawtooth crashes, while trapped fast ions were weakly affected [30]. The tangentially-viewing SSNPA, which is mainly sensitive to passing fast ions, observed large signal spikes at the sawtooth crashes (Fig. 8d) because fast ions moved to the edge and charge exchanged with edge neutrals. The radially-viewing SSNPA data suggest that there was a small drop of trapped particles in the core (Fig. 8e). The tangentially-viewing FIDA (t-FIDA) system, which is sensitive to passing fast ions, observed a depletion as large as 25% inside the inversion radius, but an increase at the outer region (Fig. 8d,e).

TRANSP simulations with the Kadomstev and Porcelli sawtooth models were performed. While the Kadomtsev model, which assumes full reconnection of the flux inside the q=1 surface, overestimates the neutron rate drop at each sawtooth event, the partial reconnection Porcelli model qualitatively reproduced the neutron rate drop when tuning the sawtooth model parameters. However, both sawtooth models cannot fully reproduce the observations of the t-FIDA signal change. The discrepancy suggests that the models presently implemented in TRANSP may be too simple to capture details of the variation of the fast ion distribution induced by sawteeth. In particular, introducing phase space selectivity for sawtooth induced fast ion redistribution may be required. The particle-following code ORBIT has been used to characterize the redistribution of fast particles as a function of their parameters such as energy, pitch, and radial location. Due to a sawtooth crash, as expected, the redistribution of fast ions in real space shows that fast particles with different orbit types are affected differently by the sawtooth instability, as observed in experiments. Initial interpretative TRANSP simulations using the kick model [16, 17] based on the ORBIT modeling results show features in the fast ion redistribution before/after a sawtooth crash that resemble the experimental data, as shown in Fig. 9 [31, 32]. With the fast ion distribution from the kick model, the simulated t-FIDA spatial profile qualitatively reproduces the t-FIDA observations especially the increase near the edge (Fig. 9a, d). Those features cannot be reproduced by either full or partial reconnection models (Fig. 9b, c).

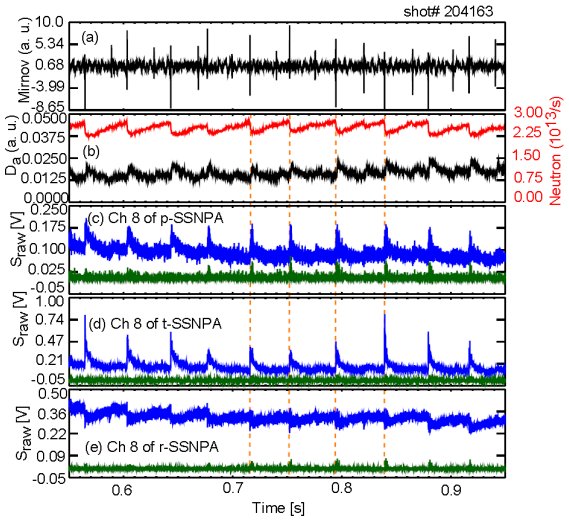

Fig. 8 Temporal evolution of (a) Mirnov coil signals, (b) neutron emission and D_α radiance from the edge of the plasma, (c) signal of passive-SSNPA, (d) signal of tangentially-viewing SSNPA and (e) signal of radially-viewing SSNPA. Reprinted from [30].

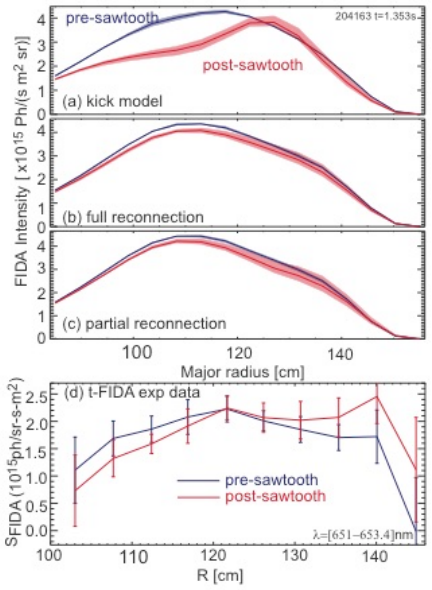

Fig. 9 Comparison of t-FIDA spatial profiles calculated by FIDAsim using the plasma profiles and fast ion distribution from (a) the kick mode, (b) the Kadomstev full reconnection model, (c) the Porcelli partial reconnection model. The measured t-FIDA profiles are shown in (d).

3. MACROSTABILITY

3.1. Neoclassical Tearing Modes

Tearing-type modes with $n = 1, m = 2$ helicity have been observed on both NSTX and NSTX-U. As observed on NSTX, soft X-ray measurements indicate coupling to a core-localized $n = 1, m = 1$ perturbation, leading to flattening of the rotation profile from the core to the $q = 2$ surface. In the discharges studied, the magnetic mode amplitude grows smoothly from the Mirnov array noise floor width, which is comparable to the ion gyro-radius. The gradual mode onset is indicative of a 'spontaneous' mode, as opposed to the paradigmatic 'neoclassical tearing mode' onset (in which the mode is metastable and is triggered instantaneously at finite amplitude by an exogenous magnetic perturbation). Prior to the emergence of the mode amplitude definitively above the noise floor, a faint precursor fluctuation is seen in many cases (Fig. 10a, t<0.6 s). It is not yet clear whether this represents turbulent excitation of a marginally-stable mode, or a mode which is linearly unstable but saturated at very low amplitude.

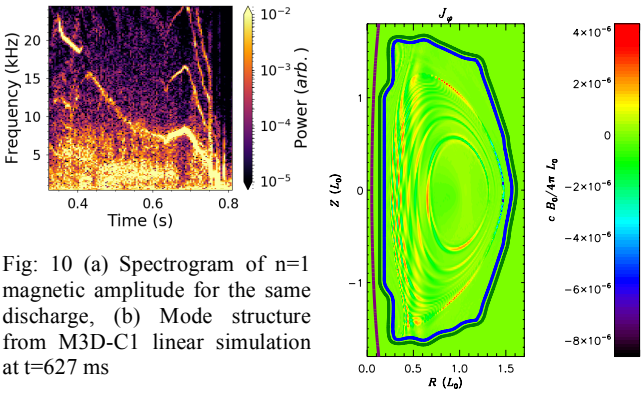

Fig: 10 (a) Spectrogram of n=1 magnetic amplitude for the same discharge, (b) Mode structure from M3D-C1 linear simulation at t=627 ms

Similar n=1 tearing mode behavior is observed in NSTX-U plasmas with higher B_T, more neutral beam heating power for similar high normalized β, and higher T_e for a longer resistive diffusion time.

Linear M3D-C1 [33] simulations indicate an instability, which comprises multiple poloidal harmonics, consistent with strong toroidicity-induced coupling at low aspect ratio (Fig. 10b). In these simulations, the mode is suppressed by inclusion of the measured plasma rotation profile, presumably due to shear. Resistive DCON stability calculations yield positive tearing stability index Δ′ well before and during the mode onset in all discharges studied. The stabilizing Glasser-Green-Johnson (GGJ) effect (due to field line curvature and pressure gradient) is thought to counteract the destabilizing Δ′. The GGJ effect increases at lower aspect ratio R/a, and is therefore expected to be more advantageously significant in NSTX/NSTX-U than standard-aspect tokamaks such as DIII-D [34]. However, the expansion of the center column in NSTX-U should weaken this stabilizing effect over that in NSTX; dedicated experiments in NSTX-U are needed to confirm this.

3.2. Disruption Prediction, Avoidance and Mitigation

DECAF [35] code development has now produced significantly increased capability by automatically identifying rotating MHD instabilities, their bifurcation, and locking. The toroidal mode number is now also automatically determined for an arbitrary number of modes occurring simultaneously. The capability has been generalized to operate on any tokamak data available to DECAF. The information analyzed for these modes along with plasma rotation profile and other plasma measurements (15 criteria presently used for analysis of NSTX) produces predictive warning signals for the modes, along with a total MHD event warning signal showing initial success as a disruption forecaster. These capabilities are illustrated for an NSTX disruption in Fig. 11. In the shot analyzed, rotating MHD instabilities thought to be non-linearly saturated and slowly evolving resistive modes are found by a generalized phase matching algorithm in DECAF using an array of toroidal magnetic probes. The code discriminates the toroidal mode number, *n*, of the instabilities and tracks all modes greater than a specified amplitude, including modes that occur simultaneously. A single "total" MHD warning signal that depends on up to 15 separate criteria, and that varies with time is also shown. A significant part of DECAF analysis is determining the best sets of criteria to choose to create a predictive DECAF warning signal. For the present model, a total warning level of 4 indicates close proximity to the disruption. The algorithm also gives us an understanding of what is happening in the plasma to create dangerous plasma states approaching the disruption. For example, early in the discharge, MHD modes are found, and core plasma rotation is low as the plasma starts up and typically transitions from counter-NBI rotation to co-NBI rotation. The mode frequencies are relatively high at this time, which is generally a safe condition. Later, near t = 0.25s, the MHD warning level increases as modes are found with decreased and decreasing rotation frequency. However, these frequencies are not critically low (no mode bifurcations are found) and plasma rotation is not low, so the warning level

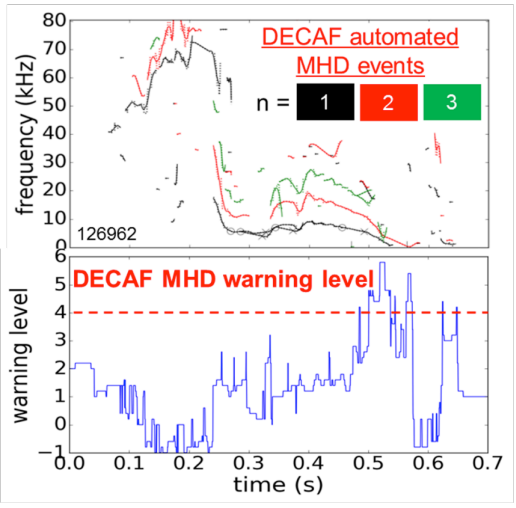

Fig. 11 DECAF decomposition of rotating MHD in a relatively slow evolution toward disruption; total MHD warning signal starts the event chain that leads to a disruption.

remains low. However, later on, more negative criteria occur simultaneously, including increased mode amplitude, decreasing mode frequencies and decreasing plasma rotation across the profile. Close to the time of the disruption, the modes drop to very low frequency, and core plasma rotation is low, leading to model locking and growth toward a critical level of locked mode amplitude. DECAF starts to show a significant change in the MHD warning level about 200 ms earlier than this, providing advanced notice of the potential disruption.

3.3. VDE modeling

Three-dimensional simulations of a vertically unstable NSTX discharge were carried out using M3D-C1 in order to investigate the formation of non-axisymmetric halo currents during a nominally axisymmetric event [36]. This work was also intended to inform the development of future halo current diagnostics on NSTX-U. These simulations were initialized with a vertically unstable equilibrium reconstruction of an NSTX discharge. In both the discharge and the simulation, the plasma control system was disabled to observe the evolution of the VDE under the condition of fixed coil currents and no disruption mitigation.

In the simulation, the plasma remains stable to non-axisymmetric modes until well after it makes contact with the wall. Once contact is made, the edge plasma is scraped off while the core plasma remains hot. While the low resistivity in the core causes the safety factor profile there to remain fixed, the contraction of the plasma current due to the scraping-off gives rise to strong skin currents at the edge which eventually become unstable, first at moderate toroidal mode numbers (n~5), and then to lower toroidal mode numbers. The non-axisymmetric halo currents due to these instabilities show a similar pattern of forming first at moderate n and coalescing to lower n. These instabilities stochasticize the edge, leading to a fast thermal quench due to parallel heat losses. Fig. 12 shows the evolution of the VDE, halo current generation and resulting jxB forces on the wall.

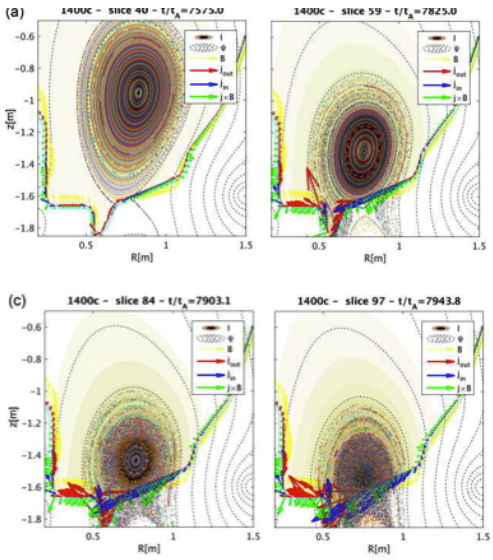

Fig. 12 Poincaré plots at a sequence of times in a 3D M3D-C1 simulation of a VDE in NSTX. Red and blue arrows show halo currents into and out of the wall, respectively. Green arrows show the direction of the poloidal electromagnetic force density on the wall.

4. EDGE AND DIVERTOR PHYSICS

4.1. SOL turbulence

Turbulence, which can influence the scrape-off layer heat flux width and thus heat flux peak values and distribution onto the plasma-facing components, has been studied in the edge and scrape-off layer of NSTX and NSTX-U coupling theory to experiment. Gas puff imaging [37] was used to characterize edge and SOL turbulence in NSTX, and 2D spatial cross-correlation studies showed the existence of time-evolving diploe-like patterns [38]. These patterns showed both negative and positive correlation structures, depending on the choice of reference location. Recent theoretical work [39] has attempted to explain these observations within the paradigm of blob-hole pair dynamics, in which blobs contain higher pressure and density than the surrounding plasma, and holes lower pressure and density. 1D and 2D correlations were determined from the theory results and compared directly to experiment.

The semi-analytic model used for this study qualitatively reproduced a number of the experimental observations. For instance, the model reproduced the dipole-like structures whose correlations flipped in sign depending on reference point position. Further, the 2D spatial correlation patters determined from the model were similar to those that were measured (Fig. 13). However, while the 2D correlations from theory showed the blob regions moving outward in time and the hole regions moving inward, the 2D correlations from experimental data showed only the former. When the experimental data maximum and minimum turbulence points (which are more sensitive and localized than the more

"averaged" 2D spatial correlations) were tracked, both the blob and the hole motion expected from theory were reproduced on average. Future work will address how these results relate to results of XGC1 calculations, which predict a significant broadening of the SOL heat flux width due to turbulence for 2 MA NSTX-U discharges [40].

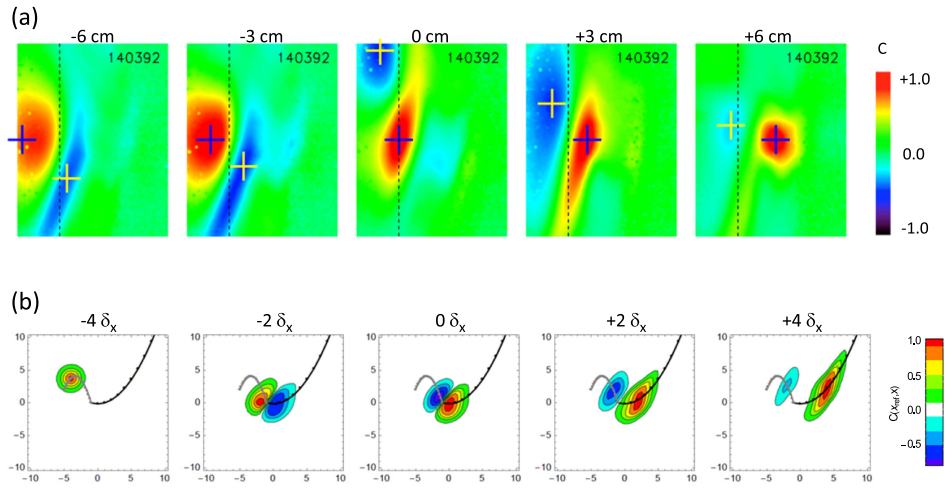

Fig. 13: Comparison of 2D spatial correlation patterns: (a) experiment and (b) theory as a function of correlation reference position (sequentially moving from closed surfaces to the SOL). Reprinted from [35].

4.2. Divertor-localized turbulence with modeling

The characterization of the structure of SOL/divertor turbulence is critical to interpret divertor measurements and transport and to understand divertor heat fluxes in present tokamaks and in ITER, where a narrow heat flux width could challenge wall materials. Recent work in NSTX-U led to the observation of *divertor leg* turbulence, where *divertor leg* indicates the region below the X-point radially limited to a few centimeters around the separatrix [41]. Filamentary fluctuations localized on the divertor legs were observed in NSTX-U L-mode discharges via fast camera imaging. The typical structure of divertor filaments is shown in Figure 14a with a rendering of flux tubes in the NSTX-U divertor corresponding to divertor localized fluctuations, and in Figure 14b with an image of the lower divertor with 9 μs exposure, showing filaments on the inner and outer divertor legs. Filaments were approximately field aligned, connected to the divertor target plate and localized to the bad curvature region on both the inner (i.e., in the private flux region) and the outer divertor legs (i.e., in the common flux region). Spatial separation (radially) between divertor leg modes and divertor turbulence due to upstream blobs was confirmed by their intersection on the divertor target plate, indicating the limited penetration of upstream modes near the separatrix. Characteristic frequencies were 10-30 kHz with filaments lifetimes of 50-100 μs and near-Gaussian probability density functions on both divertor legs. Poloidal and radial correlation lengths on the divertor legs were comparable and on the order of 10-100 ion gyroradii (1-4 cm), suggesting the local generation of these filaments. Parallel correlation lengths were ~2-3 m on both divertor legs, corresponding to more than a toroidal turn for inner leg filaments and about half of a toroidal turn for outer leg filaments. No correlation was observed with midplane turbulence. The limited parallel correlation length of both inner and outer leg turbulence can be indicative of the role of X-point disconnection.

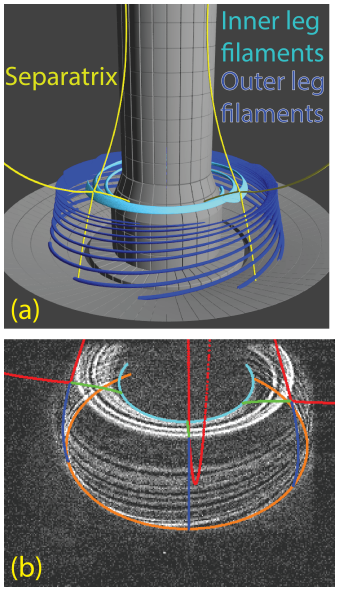

Figure 14: (a) Rendering of the NSTX-U divertor with flux tubes corresponding divertor-localized fluctuations; (b) Divertor image in C III emission (9μs exposure) after high pass filtering. Separatrix (red), inner (green) and outer (blue) divertor legs, inner (cyan) and outer (orange) strike points are overlaid.

The filament localization to the bad curvature side of divertor legs and the absence of correlation with midplane turbulence and between inner and outer legs motivated simulations performed with the ArbiTER (Arbitrary Topology Equation Reader) code [42] with a simulation grid limited to the divertor legs (between X-point and divertor target plate), separately for the inner and outer leg. Background profiles were derived from UEDGE simulations constrained by midplane experimental profiles. In both divertor legs, instabilities localized to the bad curvature side of the leg were identified and were driven by the interaction of density gradients with geodesic curvature. Outer leg modes showed growth rate saturation for higher mode numbers than inner leg modes, in qualitative consistence with experimental observations.

4.3. Divertor detachment optimization

Analysis of the divertor geometry effects in NSTX relevant to high-triangularity NSTX-U divertor configurations compared several standard lower single null divertor geometries differing mainly by the outer divertor leg length and orientation with respect to the divertor plate was summarized in [43]. Figure 15 shows the configurations compared.

The divertor poloidal leg length variation resulted in several effects, as some divertor configurations were characterized by: longer connection length (hence more parallel/perpendicular dissipation and different parallel gradients), higher degree of divertor plasma "plugging efficiency" (hence higher divertor neutral compression at lower X-point height), and higher poloidal flux expansion (resulting in much reduced deposited peak heat flux). The divertor poloidal leg orientation affected the poloidal angle at which magnetic field lines hit the divertor plate. The configurations with the angle less than 90 degrees directed recycling neutrals toward the separatrix, led to enhanced recycling and eventually to enhanced volumetric losses ("the vertical target plate" effect). In other configurations with the angle higher than 90 degrees, the neutrals were recycled toward the outer SOL and did not contribute to ionization ¸ the divertor. Re-ionization of recycling neutrals in the divertor chamber termed "flux amplification" is an essential feature of the high-recycling divertor regime. As the recycling is increased, the divertor density increased, the divertor temperature further decreased, leading to an increase in the P_{rad} and momentum loss factors, loss of parallel pressure balance, and a transition to detachment. The experimental scans were compared to two models: the two-dimensional multi-fluid plasma model with charge state resolved carbon impurity implemented in the UEDGE code, and a reduced heat flux model used for divertor heat flux estimated in NSTX-U divertor analysis. The standard divertor configurations with lower X-point height, higher connection length and low poloidal separatrix angle in NSTX appeared favorable for divertor detachment: inherently high flux expansion led to reduced peak heat flux, and plasma plugging and higher recycling lead to lower divertor temperature and higher density. Such configurations overcome unfavorable effect created by open horizontal plate divertor configuration. These configurations are naturally created in NSTX and NSTX-U with the existing (and planned) divertor coil layout.

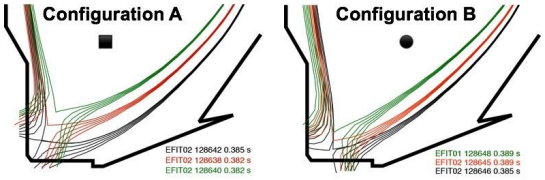

Configuration	Coils	X-pt height	R OSP
A ■	PF1AL	6-23 cm	0.30-0.39 m
B ●	PF1AL & PF1B	4-11 cm	0.42-0.45 m

Fig 15. Divertor configurations studied in NSTX [Ref. 43].

5. NSTX-U RECOVERY PLANS AND STATUS

The NSTX-U Recovery planning is ongoing, with numerous design improvements included in order to support flexible operations and increase reliability to achieve key mission goals. New requirements for the divertor heat fluxes have been defined, based on recent SOL heat flux width models. New halo currents loads have been determined based on combining data from NSTX, NSTX-U, MAST, and conventional aspect ratio devices. New error field analysis has been conducted, with the goal of optimizing both the global MHD stability and minimizing PFC heat flux asymmetries for scenarios with large poloidal flux expansion. New designs of graphite plasma facing components utilize

castellations to reduce the mechanical stresses, allowing tiles to reach surface temperature limits, ~1600 deg C. Improved divertor coil designs simplify fabrication and facilitate turn-to-turn testing. Modifications to the NSTX-U vacuum chamber to increase system reliability will eliminate one the ceramic insulators necessary for coaxial helicity injection (CHI). NSTX-U is expected to resume operations in CY2020-21.

ACKNOWLEDGEMENTS

This research was supported by U.S. DOE Contracts DE-AC02-09CH11466.

References

[1] Menard, J. S. Gerhardt, M. Bell et al., Nucl. Fusion **52** (2012) 083015
[2] Menard, J.E., et al., Nucl. Fusion **51** (2011) 103014; **56** (2016) 106023
[3] Menard, J.E., et al., Nucl. Fusion **57** (2017) 102006
[4] Battaglia, D.J., et al., Nucl. Fusion **58** (2018) 046010
[5] Ren, Y., W. Guttenfelder, S.M. Kaye, et al., Nucl. Fusion **53** (2013) 083007
[6] Wang, W., S. Ethier, Y. Ren et al., Phys. Plasmas **13** (2006) 092505; **22** (2015) 102509
[7] Diallo, A., S. Banerjee, S. Zweben et al., Nucl. Fusion **57** (2017) 066050
[8] Diamond, P.H., Y.-M. Liang, B.A. Carreras et al., Phys. Rev. Lett. **72** (1994) 2565
[9] Maingi, R., R.E. Bell, J.M. Canik, et al., Phys. Rev. Lett. **105** (2010) 135004
[10] Lestz, J.B., E.V. Belova and N.N. Gorelenkov, Phys. Plasmas **25** (2018) 042508
[11] Belova, E.V., et al., Phys. Plasmas **7** (2000) 4996; **10** (2003) 3240
[12] Gorelenkov, N.N., E. Fredrickson, E. Belova, et al., Nucl. Fusion **43** (2003) 228
[13] Fredrickson, E.D., et al., Phys. Rev. Lett. **118** 265001 (2017)
[14] Fredrickson, E.D., et al., Nucl. Fusion **58** 0820228 (2018)
[15] Wong H.V. et al., Phys. Lett. A **251 (**1999) 126
[16] Podestà M. et al , Plasma Phys. Control. Fusion **59 (**2017) 095008
[17] Podestà M. et al , Plasma Phys. Control. Fusion **56b** 055003
[18] Podestà M. et al , Nucl. Fusion **58** (2018) 082023
[19] Gorelenkov N., et al Nucl. Fusion **54** (2014) 125001
[20] Berk H.L., Breizman B.N. and Pekker M., Phys. Rev. Lett. **76** (1996) 1256
[21] Berk H.L., Breizman B.N. and Pekker M., Plasma Phys. Rep. **23** (1997) 778
[22] Lilley M.K., Breizman B.N. and Sharapov S.E., Phys. Rev. Lett. **102** (2009) 195003
[23] Duarte, V.N., et al., Nucl. Fusion **57** (2017) 054001
[24] Duarte V.N., et al., Phys. Plasmas **24** (2017) 122508
[25] Berk. H. L. et al., 26th IAEA Fusion Energy Conference (Kyoto, Japan 17–22 October 2016)
[26] Cheng C., Phys. Rep. **211** (1992) 1
[27] Lang J. and Fu G.-Y., Phys. Plasmas **18** (2011) 055902
[28] https://doi.org/10.11578/dc.20180627.4
[29] Duarte V.N., N.N. Gorelenkov, M. Schneller, et al., Nucl. Fusion **58** (2018) 082013
[30] Liu, D., et al., Nucl. Fusion **58** (2018) 082028
[31] Kim, D., et al., Nucl. Fusion **58** (2018) 082029
[32] Kim, D., et al., IAEA Fusion Energy Conference 2018
[33] Ferraro, N., S.C. Jardin and P.B. Snyder, Phys. Plasmas **17** (2010) 102508
[34] Hegna, C.C., Phys. Plasmas **6** (1999) 3980
[35] Berkery, J.W., S.A. Sabbagh, R. Bell, et al., Phys. Plasmas **24** (2017) 056103
[36] Pfefferlé et al, Phys. Plasmas **25** (2018) 056106
[37] Zweben, S.J. et al., Nucl. Fusion **56** (2015) 093055
[38] Zweben, S.J., et al., Phys. Plasmas **24** (2017) 102509
[39] Myra, J.R., S.J. Zweben and D.A. Russell, Plasma Phys. Cont. Fusion **60** (2018) 075015
[40] Chang, C.S., private communication (2018)
[41] Scotti F, et al., submitted to Nucl. Fusion (2018)
[42] Baver D A, et al., Commun. Comput. Phys. **20** (2016) 136155
[43] Soukhanovskii, V., "Divertor detachment optimization in an unfavorable open geometry horizontal target divertor configuration in NSTX and NSTX-U", presented at Int. Conf. on Plasma Surface Interactions in Controlled Fusion Devices, Princeton NJ (2018)